

Layered P2-Type $K_{0.65}Fe_{0.5}Mn_{0.5}O_2$ Microspheres as Superior Cathode for High-Energy Potassium-Ion Batteries

Tao Deng, Xiulin Fan, Ji Chen, Long Chen, Chao Luo, Xiuquan Zhou, Junhe Yang, Shiyu Zheng,* and Chunsheng Wang*

Potassium-ion batteries have been regarded as the potential alternatives to lithium-ion batteries (LIBs) due to the low cost, earth abundance, and low potential of K (−2.936 vs standard hydrogen electrode (SHE)). However, the lack of low-cost cathodes with high energy density and long cycle life always limits its application. In this work, high-energy layered P2-type hierarchical $K_{0.65}Fe_{0.5}Mn_{0.5}O_2$ (P2-KFMO) microspheres, assembled by the primary nanoparticles, are fabricated via a modified solvent-thermal method. Benefiting from the unique microspheres with primary nanoparticles, the K^+ intercalation/deintercalation kinetics of P2-KFMO is greatly enhanced with a stabilized cathodic electrolyte interphase on the cathode. The P2-KFMO microsphere presents a highly reversible potassium storage capacity of 151 mAh g^{-1} at 20 mA g^{-1} , fast rate capability of 103 mAh g^{-1} at 100 mA g^{-1} , and long cycling stability with 78% capacity retention after 350 cycles. A full cell with P2-KFMO microspheres as cathode and hard carbon as anode is constructed, which exhibits long-term cycling stability (>80% of retention after 100 cycles). The present high-performance P2-KFMO microsphere cathode synthesized using earth-abundant elements provides a new cost-effective alternative to LIBs for large-scale energy storage.

1. Introduction

Rechargeable lithium-ion batteries (LIBs) have been widely utilized in the portable electronics as energy storage medium, and now are penetrating to electronic vehicles.^[1] The replacement of a huge amount of combustion-engine powered cars by LIBs-driven electric vehicles would make the effort to reduce costs

in vain due to the limited and unevenly distributed Li sources.^[2] In addition, the rapid expansion of renewable energy market from wind, solar, hydropower, and other intermittent energy sources has also triggered growing demand for high-energy density and low-cost energy storage systems, which further stimulated broad investigation beyond the Li-ion battery technologies.^[3–5] Among these technologies, sodium-ion batteries (SIBs) and potassium-ion batteries (PIBs) are the two most promising alternatives to LIBs due to the earth-abundance and accessibility of Na and K compared with Li.^[3–8] Statistically, K and Na elements remarkably occupy 2.09 and 2.3 wt% of the earth's crust (vs 0.0017% of Li) respectively.^[3,9] However, since K has lower standard redox potential (−2.936 V vs standard hydrogen electrode (SHE)) than Na (−2.714 V), and is close to Li's potential (−3.040 V), a higher operating voltage, thus a high energy density could be delivered for

PIBs, which seems to be a more attractive choice as affordable replacement of LIBs as large-scale energy storage system.^[4,6,7]

Extensive efforts have been devoted to explore high capacity PIB anode and significant advances have been achieved in high performance anode materials.^[10–19] Among them, the carbonaceous materials (graphite,^[10,13,14] hard/soft carbon,^[12,13] and graphene^[18]) and metal (antimony,^[19] tin^[15]) and metal oxides ($K_2Ti_4O_9$)^[17] show very promising performance. Different from the wide range of options on anode materials, only a limited number of cathode materials have been reported for PIBs. The development of low-cost cathodes with superior potassium storage property is urgently needed to promote the large-scale applications of PIBs.^[4,7,10,11,20]

Layered transition-metal oxides, widely utilized in commercial LIBs, would be a reasonable choice for PIBs due to their high theoretical capacities, good structural stability, low cost, and environmentally friendly.^[18,21,22] The high reversibility of layered $K_{0.3}MnO_2$ cathode has been demonstrated by Vaalma et al.^[23] and the K-ion intercalation/deintercalation mechanism of layered $K_{0.5}MnO_2$ and $K_{0.6}CoO_2$ was investigated by Ceder and co-workers using in situ X-Ray diffraction analysis and first-principles calculations.^[21,24] Meanwhile, Mai and co-workers^[8] designed and fabricated layered- $K_{0.7}Fe_{0.5}Mn_{0.5}O_2$ nanowires as the cathode of PIBs, showing enhanced

T. Deng, Dr. X. Fan, Dr. J. Chen, Dr. L. Chen, Dr. C. Luo, Prof. C. Wang
Department of Chemical and Biomolecular Engineering
University of Maryland
College Park, MD 20742, USA
E-mail: cswang@umd.edu

Dr. X. Zhou
Department of Chemistry and Biochemistry
University of Maryland
College Park, MD 20742, USA

Prof. J. Yang, Prof. S. Zheng
School of Materials Science and Engineering
University of Shanghai for Science and Technology
Shanghai 200093, P. R. China
E-mail: syzheng@usst.edu.cn

 The ORCID identification number(s) for the author(s) of this article can be found under <https://doi.org/10.1002/adfm.201800219>.

DOI: 10.1002/adfm.201800219

electrochemical performance compared with those synthesized by direct calcination method. However, the poor K-ion transport kinetics within cathode materials due to the larger radius of K-ion (1.37 Å) than Li-ion (≈ 0.76 Å) seriously reduces the power density.^[4] In addition, the large structure change and distortion of layered framework during K-ion de/intercalation, as well as severe side reactions with electrolyte, further reduce the capacity and cycling stability.^[4,25] A special structural design of layered transition metal oxide materials is required to facilitate K-ion reaction kinetics and also reduce parasite reactions with the electrolyte.

Herein, we designed uniform P2-type $K_{0.65}Fe_{0.5}Mn_{0.5}O_2$ (denoted as P2-KFMO) microspheres, which are self-assembled by the primary nanoparticles (100–200 nm) via a modified solvent-thermal method, as a very promising cathode material of PIBs. The micro-sized secondary P2-KFMO microspheres can reduce the side reaction of P2-KFMO with electrolyte, while the nanosized primary particles can enhance the K-ion diffusion. The pores in P2-KFMO microspheres can accommodate the volume change, stabilizing passivation layer on the surface to achieve long cycle stability.^[26,27] Differing from previously reported P2-type transition-metal oxide cathodes prepared by solid-state calcination,^[23,24] the P2-KFMO microsphere synthesized through a modified solvent-thermal method presents excellent electrochemical performance toward potassium with a high reversible capacity (151 mAh g^{-1} at a current density of 20 mAh g^{-1}), fast K-ion intercalation/deintercalation kinetics, good rate performance, and remarkable cycling stability with 78% capacity retention after 350 cycles at 100 mAh g^{-1} as the cathode for PIBs. A full cell with P2-KFMO microspheres as cathode and hard carbon as anode further confirmed the superior K-storage capability, which delivers a considerable discharge capacity of 75 mAh g^{-1} at a current density of 100 mAh g^{-1} with high capacity retention of $>80\%$ after 100 cycles.

2. Results and Discussion

Figure 1 illustrates the three-step synthesis procedure of P2-KFMO microspheres including 1) synthesis of $Fe_{0.5}Mn_{0.5}CO_3$ microspheres from modified solvent-thermal

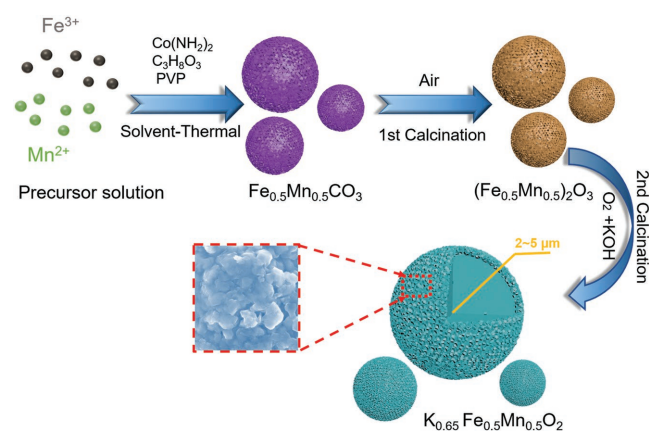


Figure 1. Schematic illustration for the synthesis of uniform P2-type $K_{0.65}Fe_{0.5}Mn_{0.5}O_2$ microspheres with hierarchical structure.

procedure, 2) conversion of $Fe_{0.5}Mn_{0.5}CO_3$ into oxides, and 3) recrystallization of oxides into P2-type $K_{0.65}Fe_{0.5}Mn_{0.5}O_2$ microspheres at elevated temperature. Detailed procedures to synthesize P2-KFMO are given in the Experimental Section. As shown in Figures S1 and S2 (Supporting Information), the X-ray diffraction (XRD) patterns of $Fe_{0.5}Mn_{0.5}CO_3$ microspheres and $(Fe_{0.5}Mn_{0.5})_2O_3$ microspheres share similar peaks with those of $MnCO_3$ and Fe_2O_3 , respectively, indicating a good Mn substitution of Fe element in the crystal structure. It is worth mentioning that after the solvent-thermal synthesis, the Fe and Mn elements are homogeneously distributed in $Fe_{0.5}Mn_{0.5}CO_3$ microspheres due to the similar cation size between the Fe (126 pm) and Mn (127 pm). The uniform distribution of Fe and Mn in the layered $K_{0.65}Fe_{0.5}Mn_{0.5}O_2$ microspheres is essential to achieve a superior electrochemical performance.^[28]

The morphologies of three products in each three-synthesis-stage ($Fe_{0.5}Mn_{0.5}CO_3$ precursor microspheres, $(Fe_{0.5}Mn_{0.5})_2O_3$ intermediate microspheres, and final P2-KFMO microspheres) are characterized using scanning electron microscopy (SEM) and are shown in Figure 2. In Figure 2a,b, the $Fe_{0.5}Mn_{0.5}CO_3$ precursor particles have a size of 4–10 μm with an ideal microspherical morphology. After the first-stage annealing in the air, the $(Fe_{0.5}Mn_{0.5})_2O_3$ intermediates that are transformed from $Fe_{0.5}Mn_{0.5}CO_3$ microparticles have similar morphology and particle size (Figure 2c,d). These $(Fe_{0.5}Mn_{0.5})_2O_3$ microspheres exhibit hierarchical structure consisting of primary particles with size of ≈ 100 nm (the inset of Figure 2d). After followed the reaction of $(Fe_{0.5}Mn_{0.5})_2O_3$ with KOH at an elevated temperature, the final P2-KFMO microspheres in Figure 2e,f still retain the spherical morphology but the recrystallization of the primary particles is enhanced. These secondary microspheres assembled by primary nanoparticles are compact and robust, which can sustain the stress/strain induced by the volume change in the K-ion intercalation and deintercalation, and accelerate the diffusion kinetics of K-ion due to the shortened K diffusion distances.^[28–30] To demonstrate the advantages of hierarchical structure on enhancing the electrochemical performance, P2-KFMO particles with irregular morphology were synthesized using a traditional solid-state method and used as a control cathode. The detailed synthesis procedures can be found in the Experimental Section. For convenience, the P2-KFMO microspheres synthesized from modified solvent-thermal method and control P2-KFMO particles synthesized using solid-state reaction were denoted as s-KFMO and c-KFMO, respectively. As showed in Figure S3a,b (Supporting Information), the c-KFMO particles have an irregular shape with a particle size of 1–2 μm , which exposes larger surface than that of s-KFMO particles.

Figure 3a shows the Rietveld refinement of the powder XRD pattern of s-KFMO particles. The background between 10° and 30° is caused by Kapton film (0.8 μm) that is used to seal the powder sample during XRD characterization. Based on our Pawley refinement, the XRD data of the prepared s-KFMO microspheres can be fit with a $P6_3/mmc$ space group with $a = 2.7184(3)$ Å and $c = 12.8289(14)$ Å. These results indicate a typical P2-type layered K-intercalated MO_2 structure, where the K ions are located at the prismatic centers of two adjacent MO_2 ($M = Fe, Mn$) sheets. The peaks labeled by asterisk around 19° , 32° were fit to a minor cubic phase with a space group of

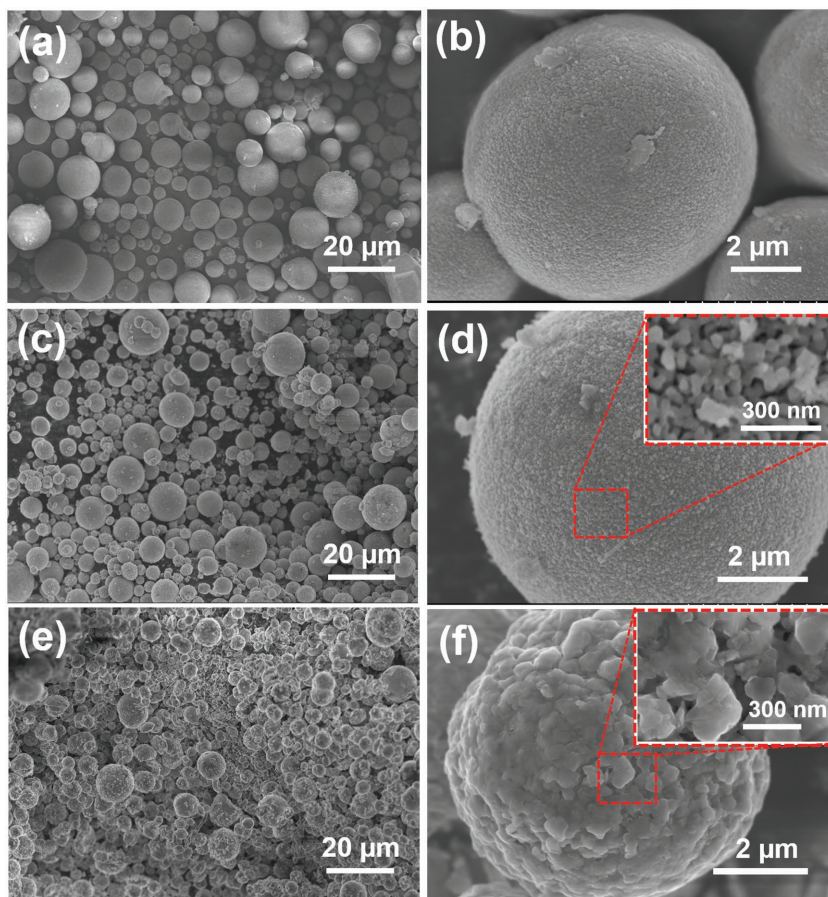


Figure 2. SEM images of as-synthesized a,b) $\text{Fe}_{0.5}\text{Mn}_{0.5}\text{CO}_3$ precursor microspheres; c,d) $(\text{Fe}_{0.5}\text{Mn}_{0.5})_2\text{O}_3$ intermediate microspheres; and e,f) P2-type $\text{K}_{0.65}\text{Fe}_{0.5}\text{Mn}_{0.5}\text{O}_2$ microspheres. The insets are the corresponding SEM images with high magnification.

Fd-3m, which is likely to be a spinel phase of Fe and Mn oxides. The inset diagrammatic presentation of Figure 3a illustrates the P2-type layered hexagonal structure of $\text{K}_{0.65}\text{Fe}_{0.5}\text{Mn}_{0.5}\text{O}_2$ microspheres. The crystalline structure of s-KFMO particles, as well as elemental distribution, was further investigated by high resolution transmission electron microscopy (HRTEM) and energy dispersive X-ray spectroscopy (EDS), as shown in Figure 3b–d. The HRTEM image shows that the hierarchical s-KFMO particles are consisting of agglomerated nanometers with well crystallinity. Meanwhile, the clear lattice fringes with a d-spacing of 0.63 nm correspond to the (002) planes of $\text{K}_{0.65}\text{Fe}_{0.5}\text{Mn}_{0.5}\text{O}_2$ (hexagonal, $P6_3/mmc$). Figure 3c presents a typical s-KFMO microsphere and the corresponding EDS elemental mapping is shown in Figure 3d. The K, Fe, Mn, and O elements are uniformly distributed on s-KFMO sample, demonstrating that the modified thermal-synthesis method is very effective to fabricate cathode material with complex hierarchical structures. The atomic ratio of K/Fe/Mn \approx 1.3:1:1 confirms the chemical composition of P2-type $\text{K}_{0.65}\text{Fe}_{0.5}\text{Mn}_{0.5}\text{O}_2$. Note that the size of K^+ is much larger than those of Li^+ and Na^+ , it is difficult to occupy more sites within the layered structures of transition-metal oxides, due to increased repulsion forces and reduced bond length between transition metal and oxygen.^[24]

The electrochemical performances of the s-KFMO cathode were investigated by cyclic voltammetry (CV) and galvanostatic charge/discharge cycling in coin cells using metal K as a counter electrode. All the coin cells for electrochemical characterization are first charged to 4.2 V (depotassiation process) and then discharged to 1.5 V (potassiation process). For CV testing, the anodic scan (oxidation process) is first performed and then followed by cathodic scan (reduction process). **Figure 4a** presents the first three CV profiles at a scanning rate of 0.1 mV s^{-1} between 1.5 and 4.2 V (vs K/K⁺). The two oxidation peaks (2.30, 2.74 V) of anodic scan and corresponding two reduction peaks (1.87, 2.45 V) of cathodic scan in the CV curves can be assigned to the low-spin $\text{Mn}^{3+}/\text{Mn}^{4+}$ redox couple.^[21] While the oxidation peak (4.02 V) and reduction peak (3.80 V) are attributed to the high spin $\text{Fe}^{3+}/\text{Fe}^{4+}$ redox couple.^[31] The electron energy loss spectroscopy (EELS) spectra results (Figure S4 and Table S1, Supporting Information) further demonstrated the existence of low-spin $\text{Mn}^{3+}/\text{Mn}^{4+}$ and high spin $\text{Fe}^{3+}/\text{Fe}^{4+}$ redox couples during discharging of P2-KFMO sample. The rapidly increased current at potential higher than 3.8 V is due to the decomposition of electrolyte since the reaction is irreversible but repeatable. Optimization of the electrolyte may suppress the decomposition reaction, thus further improve cell performance.

Similar to other P2-type oxides cathode materials of PIBs, the shapes of CV curve are also affected by the complicated phase transitions, due to the changeable states of K^+ /vacancy ordering and MO_2 layer gliding during K-ion insertion/desertion.^[3,30,32] After the initial activation cycle, the CV curves are overlapped with previous CV curves, demonstrating an excellent reversibility of the s-KFMO electrode during K-ion intercalation/deintercalation cycling.

Figure 4b shows the first five galvanostatic charge and discharge profiles of the s-KFMO cathode at a current density of 20 mA g^{-1} between 1.5 and 4.2 V (vs K/K⁺). The potential plateaus in charge and discharge profiles are consistent with CV results. The initial charge curve of s-KFMO possesses a higher overpotential due to the high stress/strain in the activation process. The K-ion intercalation in P2-layered oxides presents more slope potential plateau than those of Li-ion and Na-ion because 1) large ionic size of K causes strengthening of K–K interaction and 2) larger slab space between MO_2 layers leads to screening of K–K electrostatic interaction by oxygen.^[24,32,33] As shown in Figure 4b, specific capacities of 168 and 151 mAh g^{-1} were obtained in the first charge and discharge, respectively, with an average potential of $\approx 2.5 \text{ V}$ (vs K/K⁺). The subsequent charge and discharge profiles are totally overlapped, implying highly reversible K-ion intercalation and deintercalation processes. In addition, the galvanostatic intermittent

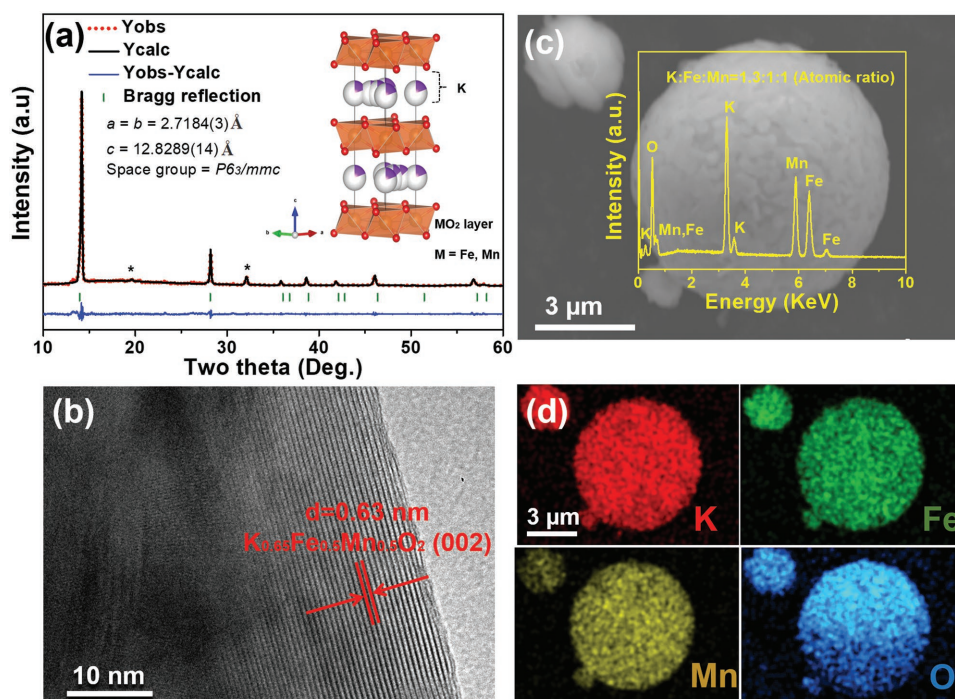


Figure 3. a) Pawley refinement of powder X-ray diffraction data, the inset is the schematic structure of P2-type $\text{K}_{0.65}\text{Fe}_{0.5}\text{Mn}_{0.5}\text{O}_2$ microspheres (s-KFMO). b) TEM image of s-KFMO particles. c) Typical SEM image of s-KFMO particles and corresponding elemental mapping of d) potassium, iron, manganese, and oxygen elements.

titration technique (GITT) was also applied to measure the quasi-equilibrium potential and maximum capacity of s-KFMO particles (Figure S5, Supporting Information). Clearly, the maximum capacity of the layered s-KFMO indicated by GITT results is around 194 mAh g^{-1} , which is close to theoretical capacity of 211 mAh g^{-1} .

The rate performances of both s-KFMO and c-KFMO cathodes were also investigated (Figure 4c). As can be seen, the s-KFMO electrode maintains reversible discharge capacities over multiple cycles at each C rate by delivering an average capacity of 149, 124, 103, 80, 56, and 34 mAh g^{-1} at a current density of 20, 50, 100, 200, 400, and 800 mA g^{-1} , respectively. When the current density is reduced back to 100 mA g^{-1} , a reversible capacity of 104 mAh g^{-1} can be recovered, indicating stable layered framework and excellent tolerance for the rapid K-ions intercalation/deintercalations. The corresponding charging/discharging curves of s-KFMO electrode at different current densities are presented in Figure 4d. However, the specific capacity of c-KFMO electrode is dramatically reduced as the current density is increased. When the current density is back to 100 mA g^{-1} , only a low discharge capacity of 80 mAh g^{-1} can be recovered, followed with a continuously capacity decay (Figure 4c; Figure S6, Supporting Information).

The severe capacity decay of c-KFMO electrode can also be observed in cycling stability testing, as shown in Figure 4e. Specifically, the discharge capacity of c-KFMO electrode decreases rapidly from 91 to 71 mAh g^{-1} after the first 5 cycles at a current of 100 mA g^{-1} . After 180 cycles, a discharge capacity is further reduced to 55 mAh g^{-1} with a low capacity retention of 60% and a low average Coulombic efficiency of $\approx 92\%$. After examining the K/c-KFMO cell after 180 cycles, we found that

the electrolyte in K/c-KFMO cell almost drought out due to the severe surface reactions with active material. By contrast, the s-KFMO electrode exhibits excellent cycling stability with a capacity retention of 78% over 350 cycles at a current density of 100 mA g^{-1} (Figure 4e), corresponding to an average capacity loss of 0.07% per cycle. The Coulombic efficiency of the electrode remains $>99\%$ after the first 30 cycles. In addition, the corresponding discharge energy density curve for s-KFMO cathode is presented in Figure S7 (Supporting Information). The initial discharge energy density can reach up to 300 Wh kg^{-1} at current rate of 100 mA g^{-1} between 1.5 and 4.2 V (vs K/K⁺). The superior potassium storage properties of s-KFMO particles in this study can be attributed to the enhanced kinetics of K-ion intercalation/deintercalation and minimization of side reactions, due to its uniform hierarchical microsphere structure. First, the primary nanoparticles can provide stable K⁺ and electron transport pathways; therefore maximize the utilization of the active materials.^[28,30,34,35] Second, the microsize of microsphere structure can effectively buffer the mechanical stress caused by K-ion intercalation/deintercalation and minimize the contacting area of the electroactive materials with electrolyte, thus preventing pulverization and reducing unwanted side reactions and therefore leading to improvement of structural stability and cycling stability.^[26,34,36]

The ex situ XRD (Figure 5a) was conducted to unveil the structural evolutions and K-ion de/intercalation mechanisms of s-KFMO particles at different states of charge (or discharge) marked in Figure 5b at a low current density of 20 mA g^{-1} . The (002), (004), as well as some adjacent peaks, which are most sensitive to the K content during charging and discharging, are used to monitor the structural evolution of P2-KFMO sample.^[21,37,32a]

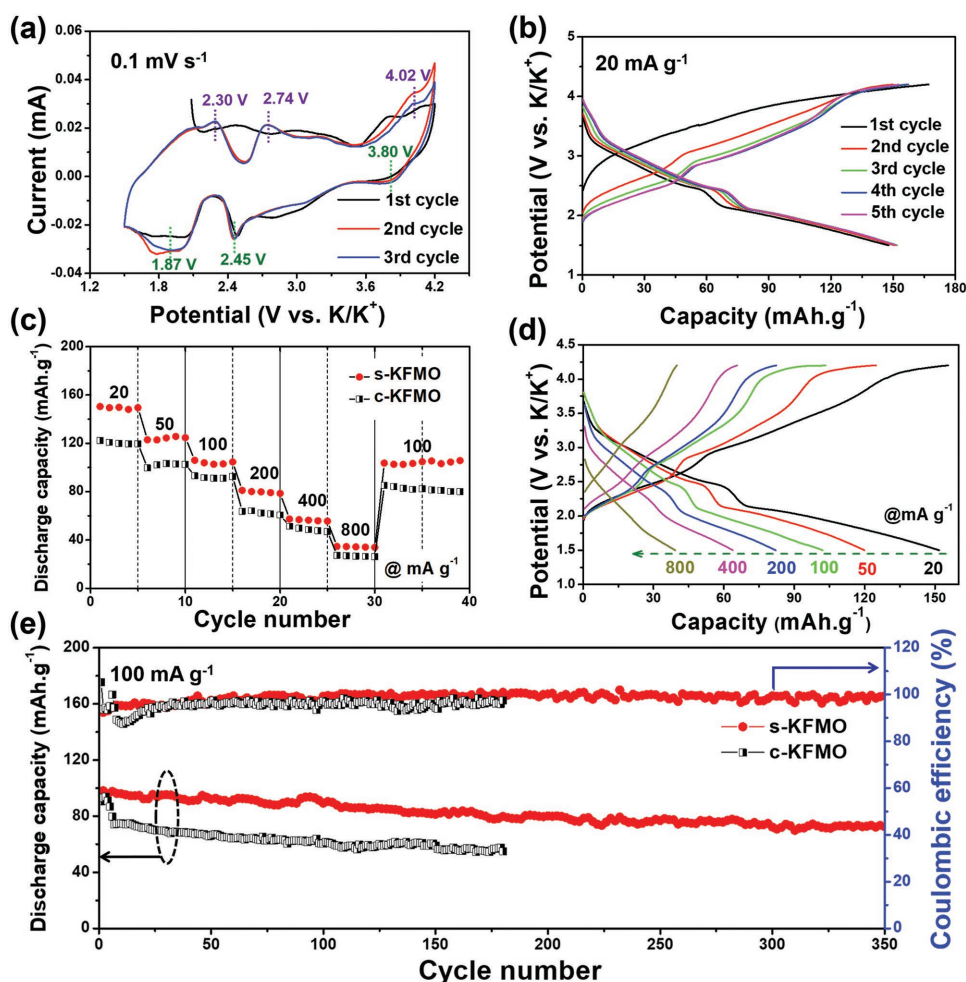


Figure 4. Electrochemical performance of P2-KFMO sample in half-cell configuration. a) CV curves for the s-KFMO electrode at a scanning rate of 0.1 mV s^{-1} . b) Electrochemical charge/discharge curves of s-KFMO cathode at a constant current of 20 mA g^{-1} . c) Rate capability of s-KFMO and c-KFMO electrodes at current rates of 20, 50, 100, 200, 400, 800 mA g^{-1} . d) Charge/discharge profiles of P2-KFMO electrode at different current densities, increasing from 20 to 800 mA g^{-1} . e) Cycling performance of s-KFMO and c-KFMO electrodes at a constant current of 100 mA g^{-1} . All of the current densities and capacities were calculated based on the weight of active material P2-KFMO. All the tests were performed in the voltage range of 1.5–4.2 V (vs K/K⁺) at room temperature.

It should be noted that some other peaks (012, 006, etc.) are difficult to be observed in Figure 5a due to the preferred orientation after charge and discharge process. The present ex situ XRD patterns show that when the potential of the electrode reaches at 4.0 V (#A, #E, #F in Figure 5b), the phase transition from hexagonal P2 phase to the O2 phase occurs upon K-ion deintercalation. Such P2–O2 transition, commonly observed in P2-type alkali transition-metal oxides, can be verified by the characteristic of PO4 phase, which is believed due to the intergrowth structure between P2-type and O2-type structure.^[37–40] The appearance of the new peak of (002') for O2 phase in the ex situ XRD pattern confirms the coexistence of two-phase for s-KFMO at high potential, which results from the gradual increasing K interslab distance due to an increasingly strong electrostatic repulsions between successive MO₂ layers.^[21,38] When s-KFMO is discharged to 1.6 V, (002), (004), and other adjacent peaks returned to the initial state of pure P2 phase, demonstrating the highly reversible phase transformation of s-KFMO electrode during K⁺ intercalation/deintercalation,

thus long cycling stability of s-KFMO electrode. Due to the phase transformation delay in the charge/discharge process, peak intensities of ex situ XRD pattern for different samples are not exactly the same. However, the P2–O2 transition of P2-KFMO sample during charging and discharging can still be demonstrated by the evolution of peak positions. Since P2 phase is much reversible than O2 phase, stabilization of the P2 phase at high potential by element doping can enhance the cycle life. Some dopant, such as Mg and Ni, has proven to be very effective to stabilize the high potential phase of P2-type cathodes for LIBs and SIBs.^[40,41]

To understand the supper cycling stability mechanism in s-KFMO particles, ex situ XRD was also performed on an electrode after 105 cycles. The ex situ XRD results presented in Figure S8 (Supporting Information) demonstrate that the crystallinity of the s-KFMO cathode still retained after 105 charge/discharge cycles. The diffraction patterns of the s-KFMO electrode after the 1st and 105th cycles are almost the same, indicating the same crystal structure of cycled active materials.

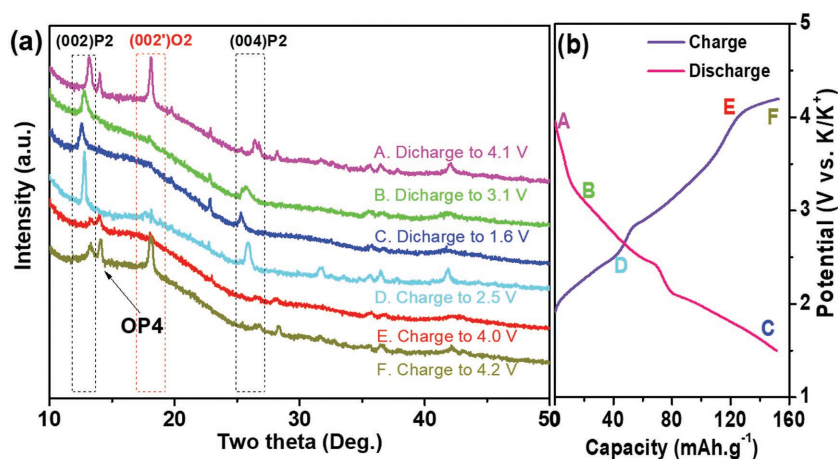


Figure 5. a) Ex situ XRD patterns to track the structural change upon K^+ intercalation and deintercalation. b) Typical galvanostatic charge/discharge profile of a s-KFMO cathode between 1.5 and 4.2 V at a current density of 20 mA g^{-1} .

Figure S9 (Supporting Information) shows the morphology of s-KFMO cathode after the 200th charge/discharge cycle. No significant change in the morphology of s-KFMO particles can be observed after repeated charge/discharge cycles, as shown in Figure S9 (Supporting Information). The original morphology of the s-KFMO particles is well-preserved. In addition, the surface of s-KFMO cathode is covered by a homogenous passivation layer (Figure S9b–d, Supporting Information), which effectively protected the inner active materials from reaction with electrolyte and helped maintain the high electronic conductivity. This stable passivation layer with a thickness of 3–5 nm was further confirmed by ex situ transmission electron microscopy (TEM) analysis of pristine s-KFMO particles and the cycled s-KFMO particles (Figure S10, Supporting Information). The formation of stable passivation layer results from the hierarchical structure of s-KFMO particles, which has high mechanical strength to prevent pulverization during potassiation and depotassiation. By contrast, Figure S3c,d (Supporting Information) shows that the c-KFMO electrode after 180 cycles presents protruding morphology with an uneven passivation layer. Apparently, some c-KFMO particles were pulverized into smaller pieces, adding additional side surface reactions with electrolyte. Therefore, both the pulverization and side reactions during charge/discharge cycling resulted in the rapid capacity decay and low Coulombic efficiency of c-KFMO electrode, shown in Figure 4e.

As K metal is much more reactive and dangerous than Li metal and Na metal, K-metal dendrite growth in K metal/P2-KFMO battery will cause more serious safety issue. Therefore, K-ion full batteries using P2-KFMO as cathode and hard carbon

as anode are more practical choice (Figure 6). In this work, the hard carbon was synthesized by carbonization of rice starch powder (Figure S11, Supporting Information),^[23,42] and the detailed synthesis processes are shown in the Experimental Section. The hard carbon anode is fabricated and utilized as anode in present work because hard carbon has not only high capacity (Figure S12, Supporting Information) and fast charge/discharge rate capability (Figure S13, Supporting Information), but also long cycling stability (Figure S14, Supporting Information). Such superior electrochemical performance of hard carbon as the anode material of PIBs has also been reported by other groups.^[12,13,23] Before assembling the full cell, the hard carbon anode was precycled between 0.01 and 2.00 V (vs K/K^+) to eliminate the large irreversible capacity in the first discharge process shown in Figure S12 (Supporting information).

The charge/discharge behavior of s-KFMO cathode and hard carbon anode during K^+ intercalation and deintercalation was evaluated in the half cell using K metal as a reference and counter electrode (Figure S15, Supporting Information). Figure 6a displays the schematic K-ion full cell configurations

(Supporting information). The charge/discharge behavior of s-KFMO cathode and hard carbon anode during K^+ intercalation and deintercalation was evaluated in the half cell using K metal as a reference and counter electrode (Figure S15, Supporting Information). Figure 6a displays the schematic K-ion full cell configurations

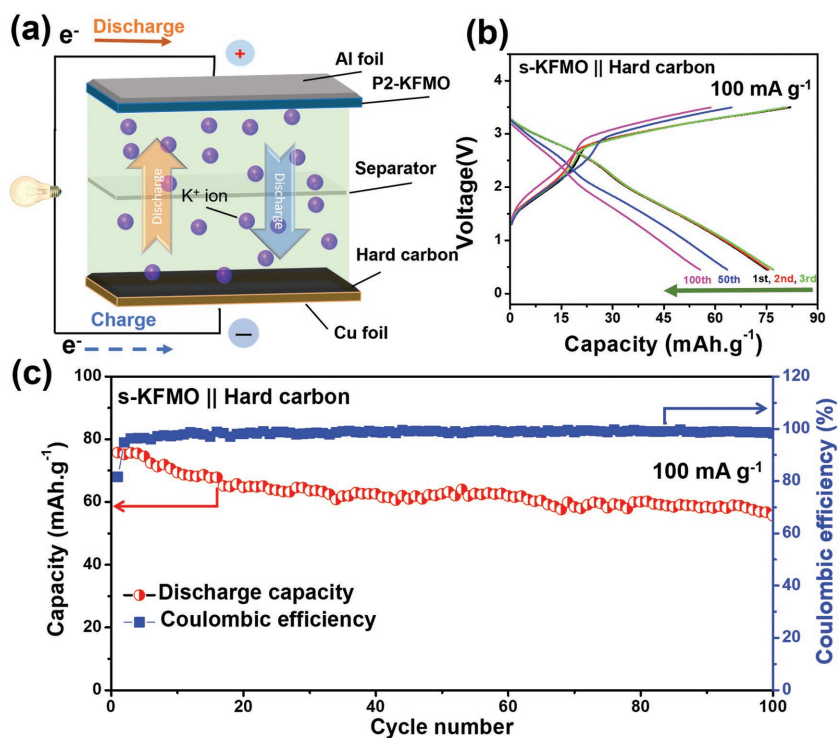


Figure 6. Demonstration of potassium-ion batteries (PIBs) based on s-KFMO || hard carbon configuration: a) Schematic illustration of the PIBs. b) Electrochemical charge–discharge voltage profiles of PIBs, cycled at a current rate of 100 mA g^{-1} . c) Cycling performance of PIBs at a constant current of 100 mA g^{-1} . All the current densities were normalized by the weight of active material on the cathode side. The full cell tests were performed in the voltage range of 0.5–3.5 V at room temperature.

with s-KFMO as cathode and hard carbon as anode. The charge–discharge profiles of s-KFMO/C full cell at a current density of 100 mA g⁻¹ between 0.5 and 3.5 V are shown in Figure 6b. The corresponding charge/discharge capacities in the first cycle can reach 82 and 76 mAh g⁻¹, respectively (normalized with the total weights of P2-KFMO and hard carbon). Besides the large capacity, the full cell also exhibits good long cyclability. As shown in Figure 6c, the full cell delivers a considerable discharge capacity of 75 mAh g⁻¹ at a current density of 100 mA g⁻¹, and the average Coulombic efficiency is higher than 99% during charge–discharge test. s-KFMO/hard carbon full cell still retains >80% of initial capacity after 100 cycles (Figure 6c). However, if normalized by the weight of cathode active material only, the initial discharge capacity of full cell increases to 95 mAh g⁻¹ with a retention of 75% after 100 cycles (Figure S16, Supporting Information).

The capacity decay of s-KFMO/hard carbon full cell during long cycling might be attributed to unstable solid-state interphase formation and the consumption of electrolyte on electrodes, which is very common for LIBs. In the long run, to further improve the electrochemical performances of s-KFMO/C full cell, new electrolytes, as well as additives, should be developed to match well with both s-KFMO cathode and hard carbon anode. Although the electrochemical properties of the full cell require further improvement to meet the need of real application, the preliminary results have demonstrated the potential of earth-abundant s-KFMO as the cathode candidate of PIBs for large-scale energy storage systems.

In general, the excellent electrochemical performance and structure stability of s-KFMO electrode can be attributed to its unique hierarchical structures. First, the nanosized s-KFMO primary particles afford a stable K-ions and electron transport pathway, enhancing reaction kinetics and utilization of the active material upon discharge and charge. Second, the secondary microsphere structure decreases contact area of the active materials with electrolyte, thus reducing unwanted side reactions and active materials dissolution and leading to high Coulombic efficiency.^[26,30,36] Third, the uniformly formed passivation layer on the surface of s-KFMO cathode further alleviates the side reactions at the interface between microspheres and the electrolyte, resulting in the structural and interfacial stability of s-KFMO electrode. This feature is especially important for the P2-type transition-metal oxides for PIBs, since the side reaction between transition metals and electrolytes usually causes the fast decay of the reversibility.^[3,4,26,32] The above synergetic effect ensures an impressive potassium storage performance with high reversible capacity and superior cycling stability of s-KFMO cathode in both half-cell and K-ion full batteries.

3. Conclusion

In summary, we designed and synthesized the uniform layered P2-type K_{0.65}Fe_{0.5}Mn_{0.5}O₂ microspheres via refined solvent-thermal method as cathode material for potassium-ion batteries. The P2-KFMO microspheres (s-KFMO, 4–10 μm) consist of the primary nanoparticles (≈100 nm), which provide shortened ion diffusion distance, good electronic conductivity, superior structure robustness against strain and stress induced

by K-ion intercalation/deintercalation, as well as minimal contact area between cathode material and electrolyte. The as-synthesized s-KFMO particle exhibits a highly reversibility with a high capacity of 151 mAh g⁻¹ (20 mA g⁻¹), and good cycling performance with 78% capacity retention after 350 cycles, which is one of the best layered transition-metal oxide cathode ever reported for PIBs. A s-KFMO full cell paired with a hard carbon anode further demonstrates the impressive electrochemical performance with a long-term cycling stability (>80% of retention after 100 cycles). The present high-performance K-ion battery with s-KFMO as cathode, in which all of the elements are earth-abundant, provides a new cost-effective alternative to LIBs for large-scale energy storage applications.

4. Experimental Section

Material Synthesis: All the reagents were purchased from Sigma-Aldrich and used as received. To synthesize the P2-type K_{0.65}Fe_{0.5}Mn_{0.5}O₂ microspheres electrode, the Fe_{0.5}Mn_{0.5}CO₃ precursors were first prepared according to a previously reported method with minor modification.^[30] In a typical synthesis, 473.0 mg of FeCl₃·6H₂O (>99%), plus 346.4 mg MnCl₂·4H₂O (>99%, Fe/Mn = 1 in molar ratio), was dissolved into solution containing 70 mL of distilled water, 2.46 g of urea, 2.5 g of ascorbic acid, and 2 g of polyvinylpyrrolidone (MW ≈ 40 K). After stirring and mixing well, the mixture was transferred into a 100 mL Teflon-lined stainless steel autoclave and maintained at 160 °C for 6 h in a laboratory oven. The Fe_{0.5}Mn_{0.5}CO₃ microspheres were obtained after being centrifuged and washed with water/ethanol for several times and dried at 60 °C overnight. Then, the precursor Fe_{0.5}Mn_{0.5}CO₃ microspheres were calcinated in air at 400 °C for 5 h to obtain the (Fe_{0.5}Mn_{0.5})₂O₃ microspheres as intermediates of final P2-type K_{0.65}Fe_{0.5}Mn_{0.5}O₂ microspheres. After the calcination, the (Fe_{0.5}Mn_{0.5})₂O₃ microspheres and KOH (5% of excess) were well dispersed in distilled water with a molar ratio of 1:0.68. The prepared suspension was dried at 80 °C overnight. Finally, the collected solid composites were heated at 350 °C for 2 h and 1000 °C for 10 h in O₂ environment to obtain the final product of P2-K_{0.65}Fe_{0.5}Mn_{0.5}O₂ microspheres. After natural cooling, the temperature was held at 200 °C before the samples were collected in argon-filled glovebox to prevent contamination from moisture in the air.

As a reference, the P2-type K_{0.65}Fe_{0.5}Mn_{0.5}O₂ particles were synthesized using a simple solid-state reaction from stoichiometric amounts of KOH, Fe₂O₃, and Mn₂O₃ powder with molar ratios of 2/3:1/4:1/4. The mixtures of the samples were thoroughly ground by a mortar and pestle. Then, the obtained solid mixture was pelletized and heated at 1000 °C for 12 h in air with a heating rate of 2 °C min⁻¹. Finally, when the temperature was held at 200 °C, the samples were quickly transferred to an argon-filled glovebox for further characterization.

Hard carbon (HC) was synthesized by thermal decomposition of starch powder from rice, which has been reported in previous literature.^[23,42] In detail, the rice starch was first preheated in a muffle furnace at 503 K (230 °C) for 5 h with a heating rate of 1 K min⁻¹ under air atmosphere. Then, the collected black grains were ground and fired in a tube furnace under argon atmosphere. During heating, a large Ar flow rate of 105 cm³ min⁻¹ was needed to prevent further decomposition of precursors. After the temperature increased to 1373 K (1100 °C, 1 K min⁻¹) and was held for 1 h, keep the material was furnace-cooled to room temperature under the argon flow condition. The black HC powder in the end was obtained and used without further purification.

Material Characterizations: SEM and TEM images in present work were taken by Hitachi SU-70 analytical SEM (Japan) and JEOL (Japan) 2100F field emission TEM, respectively. The Powder X-ray diffraction (PXRD) data were collected with a Bruker D8 X-ray diffractometer using Cu Kα radiation (λ = 1.5418 Å). EELS spectra were obtained from thin specimens on a JEOL 2100F equipped with Gatan spectrometer, using parallel incident electron beam and semicollection angle of 8 mrad in

TEM diffraction mode. Before each PXRD measurement, the sample was sealed by thin Kapton film (0.8 μm) in an Ar-filled glove box to avoid degradation by moisture. Pawley refinements of PXRD data were carried out using the TOPAS 4.2 software.^[43] During the measurement of ex situ XRD patterns for tracking the structural change of $K_{0.65}Fe_{0.5}Mn_{0.5}O_2$, the sample of free-standing P2-KFMO electrode were prepared by mixing of 80% active material, 10% carbon black, and 10% polytetrafluoroethylene. The cycled composite electrodes were rinsed with diethyl carbonate (DEC) to remove excess electrolyte, and then dried at room temperature in the Ar-filled glove box under vacuum. The cycled composite electrode powder was sealed using a Kapton film in the glove box to prevent sample exposure to air. The morphological features of the cycled samples were also observed using Hitachi SU-70 analytical SEM.

Electrochemical Measurements: The electrochemical tests in this paper were performed using a coin-type half-cells (CR 2032). Electrodes were prepared by mixing the as-synthesized P2-type $K_{0.65}Fe_{0.5}Mn_{0.5}O_2$, super P carbon black, and polyvinylidene fluoride (PVDF) binder (mass ratio of 5:1:1) with N-methyl-2-pyrrolidone (NMP) into a homogeneous slurry using a pestle and mortar in an Ar-filled glove box to prevent contamination from moisture. The slurry mixture was then coated onto aluminum foil and finally dried at 100 °C for 24 h under vacuum for further utilization. The hard carbon anode was prepared by mixing hard carbon (80 wt%), super P carbon black (10 wt%), and dry PVDF (10 wt%) with NMP. The mixture was then coated onto copper foil and dried at 100 °C for 24 h under vacuum. For the half-cell testing, coin cells (2032-type) were assembled in the glove box with a two-electrode configuration using K metal as a counter electrode. The electrolyte solution was comprised of 0.9 M KPF₆ in ethylene carbonate:DEC (1:1 by volume). The cells were assembled with a glass microfiber filter film (Whatman GF/F, USA) as the separator. Cathode films with loading densities of ≈2 mg cm⁻² were electrochemically tested on an Arbin battery test station (BT2000, Arbin Instruments, USA). Specific capacities calculations were based the mass of active species of P2-type $K_{0.65}Fe_{0.5}Mn_{0.5}O_2$. For the full cell test, a hard carbon anode was initially cycled between 0.01 and 2.0 V (vs K/K⁺) to remove the portion of irreversible capacity from the first cycle. The full cell was assembled with the P2-type $K_{0.65}Fe_{0.5}Mn_{0.5}O_2$ cathode and a cycled HC anode. To ensure a suitable cathode-to-anode capacity ratio for proper cell balance, cathode-limited configuration was chosen with a cathode-to-anode mass loading ratio of ≈2.1:1. This weight ratio of active materials for two electrodes was balanced referenced to the corresponding reversible capacity. The energy density of the cathode was calculated by integration of voltage of cathode with capacity which is automatically recorded from the Arbin Instruments.

Supporting Information

The Supporting Information is available from the Wiley Online Library or from the author.

Acknowledgements

T.D. and X.F. contributed equally to this work. The authors thank the support from the Nanostructures for Electrical Energy Storage (NEES), an Energy Frontier Research Center funded by the U.S. Department of Energy, Office of Science, Basic Energy Sciences under Award number DESC0001160. The authors gratefully acknowledge the support of the Maryland NanoCenter and its AIM Lab.

Keywords

earth-abundant cathode materials, energy storage, $K_{0.65}Fe_{0.5}Mn_{0.5}O_2$, layered transition-metal oxides, potassium-ion batteries

Received: January 9, 2018
Revised: May 2, 2018
Published online:

- [1] a) J. Hassoun, S. Panero, P. Reale, B. Scrosati, *Adv. Mater.* **2009**, *21*, 4807; b) B. Scrosati, J. Hassoun, Y.-K. Sun, *Energy Environ. Sci.* **2011**, *4*, 3287; c) J. B. Goodenough, K. S. Park, *J. Am. Chem. Soc.* **2013**, *135*, 1167.
- [2] a) H. D. Yoo, I. Shterenberg, Y. Gofer, G. Gershinsky, N. Pour, D. Aurbach, *Energy Environ. Sci.* **2013**, *6*, 2265; b) Y. Zhu, S. H. Choi, X. Fan, J. Shin, Z. Ma, M. R. Zachariah, J. W. Choi, C. Wang, *Adv. Energy Mater.* **2017**, *7*, 1601578; c) X. Fan, J. Mao, Y. Zhu, C. Luo, L. Suo, T. Gao, F. Han, S.-C. Liou, C. Wang, *Adv. Energy Mater.* **2015**, *5*, 1500174.
- [3] N. Yabuuchi, K. Kubota, M. Dahbi, S. Komaba, *Chem. Rev.* **2014**, *114*, 11636.
- [4] A. Eftekhari, Z. Jian, X. Ji, *ACS Appl. Mater. Interfaces* **2017**, *9*, 4404.
- [5] M. H. Han, E. Gonzalo, G. Singh, T. Rojo, *Energy Environ. Sci.* **2015**, *8*, 81.
- [6] A. Eftekhari, *J. Power Sources* **2003**, *117*, 249.
- [7] A. Eftekhari, *J. Power Sources* **2004**, *126*, 221.
- [8] X. Wang, X. Xu, C. Niu, J. Meng, M. Huang, X. Liu, Z. Liu, L. Mai, *Nano Lett.* **2017**, *17*, 544.
- [9] a) H. Kang, Y. Liu, K. Cao, Y. Zhao, L. Jiao, Y. Wang, H. Yuan, *J. Mater. Chem. A* **2015**, *3*, 17899; b) R. Carmichael, *Handbook of Physical Properties of ROCKS*, CRC Press Inc., Boca Raton **1982**.
- [10] a) K. Beltrop, S. Beuker, A. Heckmann, M. Winter, T. Placke, *Energy Environ. Sci.* **2017**, *10*, 2090; b) B. Ji, F. Zhang, X. Song, Y. Tang, *Adv. Mater.* **2017**, *29*, 1700519.
- [11] C. Zhang, Y. Xu, M. Zhou, L. Liang, H. Dong, M. Wu, Y. Yang, Y. Lei, *Adv. Funct. Mater.* **2017**, *27*, 1604307.
- [12] a) Z. Jian, S. Hwang, Z. Li, A. S. Hernandez, X. Wang, Z. Xing, D. Su, X. Ji, *Adv. Funct. Mater.* **2017**, *27*, 1700324; b) Z. Jian, Z. Xing, C. Bommier, Z. Li, X. Ji, *Adv. Energy Mater.* **2016**, *6*, 1501874.
- [13] Z. Jian, W. Luo, X. Ji, *J. Am. Chem. Soc.* **2015**, *137*, 11566.
- [14] a) S. Komaba, T. Hasegawa, M. Dahbi, K. Kubota, *Electrochem. Commun.* **2015**, *60*, 172; b) W. Luo, J. Wan, B. Ozdemir, W. Bao, Y. Chen, J. Dai, H. Lin, Y. Xu, F. Gu, V. Barone, L. Hu, *Nano Lett.* **2015**, *15*, 7671; c) Z. Tai, Q. Zhang, Y. Liu, H. Liu, S. Dou, *Carbon* **2017**, *123*, 54.
- [15] I. Sultana, T. Ramireddy, M. M. Rahman, Y. Chen, A. M. Glushenkov, *Chem. Commun.* **2016**, *52*, 9279.
- [16] a) Y. Xie, Y. Chen, L. Liu, P. Tao, M. Fan, N. Xu, X. Shen, C. Yan, *Adv. Mater.* **2017**, *4*, 1600343; b) N. Xiao, W. D. McCulloch, Y. Wu, *J. Am. Chem. Soc.* **2017**, *139*, 9475; c) W. Wang, J. Zhou, Z. Wang, L. Zhao, P. Li, Y. Yang, C. Yang, H. Huang, S. Guo, *Adv. Energy Mater.* **2017**, *8*, 1701648.
- [17] J. Han, M. Xu, Y. Niu, G.-N. Li, M. Wang, Y. Zhang, M. Jia, C. m. Li, *Chem. Commun.* **2016**, *52*, 11274.
- [18] K. Share, A. P. Cohn, R. Carter, B. Rogers, C. L. Pint, *ACS Nano* **2016**, *10*, 9738.
- [19] W. D. McCulloch, X. Ren, M. Yu, Z. Huang, Y. Wu, *ACS Appl. Mater. Interfaces* **2015**, *7*, 26158.
- [20] a) P. Padigi, J. Thiebes, M. Swan, G. Goncher, D. Evans, R. Solanki, *Electrochim. Acta* **2015**, *166*, 32; b) L. Xue, Y. Li, H. Gao, W. Zhou, X. Lu, W. Kaveevitvichai, A. Manthiram, J. B. Goodenough, *J. Am. Chem. Soc.* **2017**, *139*, 2164; c) Q. Zhao, Y. Hu, K. Zhang, J. Chen, *Inorg. Chem.* **2014**, *53*, 9000. d) J. Meng, H. Guo, C. Niu, Y. Zhao, L. Xu, Q. Li, L. Mai, *Joule* **2017**, *1*, 522; e) T. Deng, X. Fan, C. Luo, J. Chen, L. Chen, S. Hou, N. Eidson, X. Zhou, C. Wang, *Nano Lett.* **2018**, *18*, 1522.
- [21] H. Kim, D. H. Seo, J. C. Kim, S. H. Bo, L. Liu, T. Shi, G. Ceder, *Adv. Mater.* **2017**, *29*, 1702480.
- [22] X. Wang, P. Hu, C. Niu, J. Meng, X. Xu, X. Wei, C. Tang, W. Luo, L. Zhou, Q. An, L. Mai, *Nano Energy* **2017**, *35*, 71.
- [23] C. Vaalma, G. A. Giffin, D. Buchholz, S. Passerini, *J. Electrochem. Soc.* **2016**, *163*, A1295.
- [24] H. Kim, J. C. Kim, S.-H. Bo, T. Shi, D.-H. Kwon, G. Ceder, *Adv. Energy Mater.* **2017**, *7*, 1700098.

- [25] C. Ling, J. Chen, F. Mizuno, *J. Phys. Chem. C* **2013**, *117*, 21158.
- [26] J. Y. Hwang, S. M. Oh, S. T. Myung, K. Y. Chung, I. Belharouak, Y. K. Sun, *Nat. Commun.* **2015**, *6*, 6865.
- [27] J. Mao, C. Luo, T. Gao, X. Fan, C. Wang, *J. Mater. Chem. A* **2015**, *3*, 10378.
- [28] G. Zhu, J. Yang, Y. Liu, X. Xie, Z. Ji, J. Yin, X. Shen, *Prog. Nat. Sci.: Mater. Int.* **2016**, *26*, 264.
- [29] X. Fan, Y. Zhu, C. Luo, L. Suo, Y. Lin, T. Gao, K. Xu, C. Wang, *ACS Nano* **2016**, *10*, 5567.
- [30] Y. Fang, X. Y. Yu, X. W. D. Lou, *Angew. Chem., Int. Ed.* **2017**, *56*, 5801.
- [31] a) N. Yabuuchi, M. Kajiyama, J. Iwatate, H. Nishikawa, S. Hitomi, R. Okuyama, R. Usui, Y. Yamada, S. Komaba, *Nat. Mater.* **2012**, *11*, 512; b) J. Xu, S.-L. Chou, J.-L. Wang, H.-K. Liu, S.-X. Dou, *ChemElectroChem* **2014**, *1*, 371; c) Y. Takeda, K. Nakahara, M. Nishijima, N. Imanishi, O. Yamamoto, M. Takano, R. Kanno, *Mater. Res. Bull.* **1994**, *29*, 659; d) D. Yuan, X. Hu, J. Qian, F. Pei, F. Wu, R. Mao, X. Ai, H. Yang, Y. Cao, *Electrochim. Acta* **2014**, *116*, 300.
- [32] R. Berthelot, D. Carlier, C. Delmas, *Nat. Mater.* **2011**, *10*, 74.
- [33] S.-H. Bo, X. Li, A. J. Toumar, G. Ceder, *Chem. Mater.* **2016**, *28*, 1419.
- [34] Y. Tao, W. Gibbons, Y. Hwang, R. Radermacher, C. Wang, *Chem. Commun.* **2017**, *53*, 5637.
- [35] S. A. Cho, Y. J. Jang, H.-D. Lim, J.-E. Lee, Y. H. Jang, T.-T. H. Nguyen, F. M. Mota, D. P. Fenning, K. Kang, Y. Shao-Horn, D. H. Kim, *Adv. Energy Mater.* **2017**, *7*, 1700391.
- [36] Y. Fang, Q. Liu, L. Xiao, X. Ai, H. Yang, Y. Cao, *ACS Appl. Mater. Interfaces* **2015**, *7*, 17977.
- [37] D. Yuan, X. Hu, J. Qian, F. Pei, F. Wu, R. Mao, X. Ai, H. Yang, Y. Cao, *Electrochim. Acta* **2014**, *116*, 300.
- [38] G.-L. Xu, R. Amine, Y.-F. Xu, J. Liu, J. Gim, T. Ma, Y. Ren, C.-J. Sun, Y. Liu, X. Zhang, S. M. Heald, A. Solhy, I. Saadoune, W. L. Mattis, S.-G. Sun, Z. Chen, K. Amine, *Energy Environ. Sci.* **2017**, *10*, 1677.
- [39] J. Billaud, G. Singh, A. R. Armstrong, E. Gonzalo, V. Roddatis, M. Armand, T. Rojo, P. G. Bruce, *Energy Environ. Sci.* **2014**, *7*, 1387.
- [40] E. Talaie, V. Duffort, H. L. Smith, B. Fultz, L. F. Nazar, *Energy Environ. Sci.* **2015**, *8*, 2512.
- [41] a) P. F. Wang, Y. You, Y. X. Yin, Y. S. Wang, L. J. Wan, L. Gu, Y. G. Guo, *Angew. Chem., Int. Ed. Engl.* **2016**, *55*, 7445; b) G. Singh, N. Tapia-Ruiz, J. M. Lopez del Amo, U. Maitra, J. W. Somerville, A. R. Armstrong, J. Martinez de Ilarduya, T. Rojo, P. G. Bruce, *Chem. Mater.* **2016**, *28*, 5087.
- [42] D. A. S. a. J. R. Dahn, *J. Electrochem. Soc.* **2000**, *147*, 3.
- [43] R. W. Cheary, A. Coelho, *J. Appl. Crystallogr.* **1992**, *25*, 109.